AGU ADVANCING EARTH AND SPACE SCIENCES

AGU Advances

RESEARCH ARTICLE
10.1029/2024AV001555

Peer Review The peer review history for this article is available as a PDF in the Supporting Information.

Key Points:

- To uncover the relation between the mean flow and storm growth, we analyze Lagrangianly all midlatitude storms from 83 years of ERA-5 data
- While the Lagrangian growth rate is found to increase monotonically with baroclinicity, the storm growth time exhibits an opposite trend
- We propose a quantitative nonlinear relation between the local mean flow characteristics of the atmosphere and the mean intensity of storms

Supporting Information:

Supporting Information may be found in the online version of this article.

Correspondence to:

O. Hadas,
or.hadas@weizmann.ac.il

Citation:

Hadas, O., & Kaspi, Y. (2025). A lagrangian perspective on the growth of midlatitude storms. *AGU Advances*, *6*, e2024AV001555. https://doi.org/10.1029/2024AV001555

Received 17 OCT 2024
Accepted 27 FEB 2025

Author Contributions:

Conceptualization: Or Hadas, Yohai Kaspi
Formal analysis: Or Hadas
Funding acquisition: Yohai Kaspi
Investigation: Or Hadas, Yohai Kaspi
Methodology: Or Hadas, Yohai Kaspi
Software: Or Hadas
Supervision: Yohai Kaspi
Validation: Or Hadas
Visualization: Or Hadas
Writing – original draft: Or Hadas, Yohai Kaspi

A Lagrangian Perspective on the Growth of Midlatitude Storms

Or Hadas[1] **and Yohai Kaspi**[1]

[1]Department of Earth and Planetary Sciences, Weizmann Institute of Science, Rehovot, Israel

Abstract Extratropical storms dominate midlatitude climate and weather and are known to grow baroclinically and decay barotropically. Traditionally, quantitative climatic measures of storm activity have been mostly based on Eulerian measures, taking into account the mean state of the atmosphere and how those affect Eulerian eddy activity, but they do not consider the Lagrangian growth of the storms themselves. Here, using ERA-5 reanalysis data and tracking all extratropical storms (cyclones and anticyclones) from 83 years of data, we examine the actual growth of the storms and compare it to the Eulerian characteristics of the background state as the storms develop. In the limit of weak baroclinicity, we find that baroclinicity provides a good measure for storm maximum intensity. However, this monotonic relationship breaks for high baroclinicity levels. We show that although the actual growth rate of individual storms monotonically increases with baroclinicity, the reduction in maximum intensity at high baroclinicity is caused by a decrease in storm growth time. Based on the Lagrangian analysis, we suggest a nonlinear correction to the traditional linear connection between baroclinicity and storms' activity. Then, we show that a simplified model of storm growth, incorporating the baroclinicity effect on the vertical tilt of anomalies, reproduces the observed nonlinear relationship. Expanding the analysis to include the mean flow's barotropic properties highlights their marginal effect on storm growth rate, but the crucial impact on growth time. Our results emphasize the potential of Lagrangianly studying storm dynamics to advance understanding of the midlatitude climate.

Plain Language Summary The midlatitude climate is shaped by storms. Their growth is primarily driven by baroclinic instability, a process converting vertical wind shear into storms' energy. Understanding how climatic changes impact this growth is essential for advancing midlatitude climate and weather understanding. In this study, we systematically evaluated the growth of storms using ERA-5 reanalysis data and tracks of all storms over 83 years. The growth of individual storms is compared to baroclinicity, a widely used measure of storm activity that is primarily based on vertical wind shear. Our findings indicate that while storm intensity increases with baroclinicity under mild conditions, this relationship breaks down under extreme conditions. While the growth rate of storms continues to increase with baroclinicity, this shift is due to a decrease in the storm growth time with baroclinicity. As a result, a nonlinear correction to the traditional linear relation between baroclinicity and storm activity is proposed. Expanding the analysis to include the horizontal wind shear emphasizes its minimal impact on storm growth rate but underscores its crucial influence on growth time. These results highlight the importance of systematic study of large quantities of storms.

1. Introduction

The midlatitude momentum, heat, and moisture fluxes display significant spatial variability, primarily concentrated in regions referred to as the "storm tracks" (Chang et al., 2002; Hoskins & Hodges, 2002, 2005). Three primary storm tracks have been identified: the Northern Hemisphere (NH) Atlantic and Pacific storm tracks and the Southern Hemisphere (SH) storm track. Moreover, the midlatitude climate displays a significant temporal variability, which is primarily seasonal (Hoskins & Hodges, 2019; Nakamura & Shimpo, 2004). From an Eulerian perspective, these variations are typically quantified using climatological metrics such as Eddy Kinetic Energy (EKE, Figure 1a), which provide insights into the large-scale statistical properties of storm tracks. From a Lagrangian perspective, these spatial and temporal variabilities arise from substantial differences in cyclonic and anticyclonic activity among various parts of Earth (Figures 1b and 1c), serving as the main driver for the weather variability throughout the midlatitudes (Yau & Chang, 2020).

These variations in the storm tracks have been extensively studied, often analyzed through a three-step approach (e.g., Shaw et al., 2016). First, atmospheric flow is decomposed (via spatial or temporal filtering) into the mean

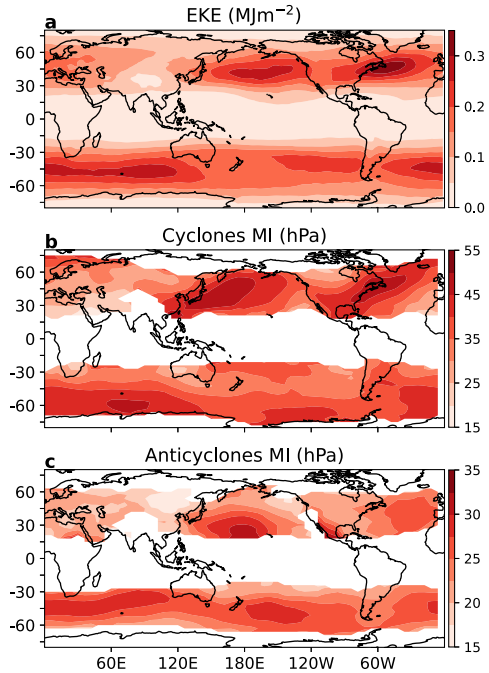

Figure 1. Climatologies of (a) vertically integrated Eddy Kinetic Energy (EKE, MJm^{-2}), and Maximum Intensity (MI, hPa, as defined in Section 2.2) of (b) cyclones, and (c) anticyclones during winter (December–January–February for the NH and June–July–August for the SH). EKE $= \equiv \frac{1}{2g}\int_{850}^{300}\left(u'^2 + v'^2\right)dp$, where p is the pressure (hPa), g is the gravitational acceleration, u' and v' are the zonal and meridional wind anomalies filtered for 2–10 days and zonal wavenumbers 4–20. The MI of each storm is counted in all grid boxes it passes through from its genesis to its MI. The MI maps' resolution is $6^\circ \times 3^\circ$, and they are smoothed using a convolution with 3×3 filter. Only grid points averaging more than 200 storms are included. Winter climatology is shown due to its strong spatial variability. These results are consistent with previous findings (e.g., Hoskins & Hodges, 2002, 2005).

flow, representing large-scale, slowly varying features like jet streams and eddy fields dominated by cyclonic and anticyclonic activity. Second, the effect of atmospheric forcing changes on the mean state is assessed, leveraging the simplification achieved through averaging. Third, the storm track response is inferred from the eddy state's reaction to mean-state changes. However, due to the nonlinear complexity of eddy fields, exact analytical solutions are unavailable, and numerical models depend heavily on specific settings. Despite these challenges, theoretical frameworks linking mean and eddy flow have been developed, including baroclinic instability models (e.g., Charney, 1947; Eady, 1949; Phillips, 1954), potential vorticity tendency decomposition (e.g., Davis & Emanuel, 1991; Hoskins et al., 1985; Tamarin & Kaspi, 2017), and energetics analyses (e.g., Lorenz, 1955; Okajima et al., 2022; Peixóto & Oort, 1974).

These methods are typically applied from an Eulerian perspective, focusing on how changes in properties of the mean flow drive climatological changes in storm tracks activity. For example, Lehmann et al. (2014) showed a strong connection between baroclinicity and EKE in CMIP5 models, and Kang et al. (2024) demonstrated that anthropogenic aerosols significantly alter mean baroclinicity, explaining much of the NH summertime circulation weakening. Beyond baroclinicity, Chemke et al. (2022) attributed the recent intensification of SH EKE—unaccounted for in CMIP6 models—to trends in the barotropic properties of the mean flow.

While the Eulerian approach has greatly advanced our understanding of midlatitude climate, it has key limitations. Averaging mean and eddy flow properties (e.g., energy conversion terms in Section 2.3) make it difficult to isolate individual contributions, limiting causal inference (Vallis, 2017). The averaging also blends the impacts of different weather systems (cyclones, anticyclones, atmospheric rivers), which have distinct dynamics. For example, comparing the climatology of EKE (Figure 1a) to the climatology of the Maximum Intensity of cyclones and anticyclones (MI, Figures 1b and 1c), reveals that cyclones tend to be strongest poleward and upstream of peak EKE, while anticyclones follow the opposite trend.

An example of a key limitation of the Eulerian perspective is the nonlinear relationship between baroclinicity and EKE. During midwinter over the Pacific, storm activity decreases even though baroclinicity is at its peak (Nakamura, 1992), a puzzle attributed to several mechanisms (e.g., Harnik & Chang, 2004; Nakamura & Sampe, 2002; Schemm & Rivière, 2019). Additionally, Haualand and Spengler (2021) found that a sharper tropopause can suppress baroclinic instability, indicating that a stronger jet does not necessarily translate to enhanced instability.

Recently, studies have addressed some of these limitations by adopting a Lagrangian perspective—tracking individual storms through space and time—to reveal key atmospheric mechanisms, improve causal inference, and better capture actual weather patterns (e.g., Hadas et al., 2023; Hadas & Kaspi, 2021; Kang & Son, 2021; Okajima et al., 2021, 2022; Okajima et al., 2024; Schemm et al., 2021; Tamarin-Brodsky & Hadas, 2019; Tamarin-Brodsky & Kaspi, 2017; Tsopouridis et al., 2021). From this perspective, the eddy mean flow interaction could be expressed in terms of how a slowly evolving climate (longer than 30 days) influences the mean dynamics of synoptic-scale storm activity (about 1 week). Although any single storm makes only a minor contribution to the mean flow, the collective impact of many storms is substantial. Therefore, understanding how the mean flow affects the mean growth of individual storms is a crucial first step toward a comprehensive Lagrangian framework for eddy–mean flow interactions, which is vital for understanding midlatitude climate.

Previous Lagrangian-based research on storm responses to the mean flow has used three main approaches: case studies (e.g., Orlanski & Katzfey, 1991; Rivière & Joly, 2006), which capture real-world processes but are limited in scope; idealized simulations (e.g., Hadas & Kaspi, 2021; Orlanski & Chang, 1993; Rivière et al., 2013), which allow for systematic investigation, but may not fully represent real conditions; and region-specific analyses (e.g.,

Okajima et al., 2023; Schemm et al., 2021; Tsopouridis et al., 2021), whose findings may be tied to local configurations.

To address these limitations, this study systematically examines how storm growth is influenced by mean flow properties commonly used in Eulerian studies. The analysis is based on 83 years of ERA-5 data (Section 2.1) and tracks extratropical storms across all seasons and regions (Section 2.2), providing a vast data set of approximately 100,000 cyclones and 50,000 anticyclones. The properties of the mean flow are characterized using the energetic perspective (Section 2.3). The analysis begins by examining the response of storm growth to the baroclinic characteristics of the mean flow (Section 3.1). These trends are then interpreted using an idealized storm growth model (Section 3.2). Finally, the analysis is extended to include the barotropic characteristics of the flow (Section 4). A brief summary of the results is provided in Section 5.

2. Methods

2.1. Reanalysis Data

Data from the European Center for Medium-Range Weather Forecasts ERA-5 reanalysis (Hersbach et al., 2020) between 1940 and 2023 is used to assess the current climate. The ERA-5 estimates atmospheric variables at a horizontal resolution of 31 km and 137 vertical levels. The three-hour Sea Level Pressure (SLP) is used to identify the tracks of cyclones and anticyclones. Three hourly temperature, geopotential, and horizontal wind data are used to characterize the mean flow. The data is down-sampled to $1.5° \times 1.5°$.

2.2. Storm Tracking and Composites

A feature point tracking algorithm (Hodges, 1995; Tamarin & Kaspi, 2016) is applied to SLP data to identify and characterize extratropical cyclones and anticyclones. The data is smoothed to T63 resolution to reduce noise, and zonal wavenumbers 0–4 are removed to isolate synoptic-scale dynamics (using the methods described in Hodges (1995)). The algorithm tracks storms by detecting local SLP minima and maxima which are associated with cyclones and anticyclones, respectively. Than, it tracks the storms, and records their position and magnitude in terms of the SLP anomaly. Storms are included if their magnitude increases for over 24 hr and they travel more than 1,000 km. Additionally, storms peaking over terrain higher than 1 km are filtered out. To maximize data availability and to make the analysis as general as possible, storms from all over the world and from all seasons are included in the analysis. The final data set includes approximately 100,000 cyclones and 50,000 anticyclones.

To quantify storm intensity, the pressure anomaly magnitude detected by the tracking algorithm is used. Since geostrophic balance implies that a given pressure anomaly corresponds to different wind strengths at different latitudes, storm intensity is defined as (e.g., Sanders & Gyakum, 1980):

$$\text{Intensity} \equiv \frac{\Delta P}{\sin(\phi)}, \tag{1}$$

where ΔP is the magnitude of the pressure anomaly identified by the tracking algorithm, and ϕ is its latitude.

Based on intensity, three measures characterizing storm growth are constructed:

- Maximum Intensity (MI, hPa)–the peak intensity reached along the track of the storm.
- Growth Time (GT, days)–the duration from genesis to maximum intensity.
- Lagrangian Growth Rate (LGR, hPa· day^{-1})–the average rate of intensification over the growth stage.

Notably, LGR does not have typical rate units (day^{-1}) because it is not normalized by the initial intensity, which is often small and highly sensitive to noise. To focus on significant events, the storms that had the 2% lowest maximum intensity were removed.

To quantify the mean flow conditions experienced by storms during growth, the mean flow is averaged spatially within a composite box extending ±2,000 km zonally and ±1,000 km meridionally from the storm's SLP anomaly center and temporarily from identification to MI.

2.3. Energetic Perspective

In this section, we define mean flow quantities that capture its fundamental properties and can be used to analyze its influence on individual storm growth. To achieve this, we adopt the energetics framework, which directly incorporates the eddy-mean flow interactions, providing a clear physical interpretation of the constructed mean flow quantities. The energy exchange between the mean flow and eddies primarily occurs through two processes: baroclinic conversion, which transfers mean available potential energy to eddy available potential energy, and barotropic conversion, which transfers eddy kinetic energy to mean kinetic energy (Lorenz, 1955).

To identify mean flow quantities that directly influence the rate of these energy conversions, we start from the equations for baroclinic and barotropic energy conversion (Simmons et al., 1983; Orlanski & Katzfey, 1991, see Appendix A for the derivation of this specific form):

$$C(P_e, P_m) = \underbrace{\frac{g}{\overline{T}\overline{N}}\left(\overline{u'T'}, \overline{v'T'}\right)}_{\text{Eddy part}} \cdot \underbrace{f\frac{}{\overline{N}}\left(\frac{\partial \overline{v}}{\partial z}, \frac{\partial \overline{u}}{\partial z}\right)}_{\text{Mean part}}, \tag{2}$$

$$C(K_e, K_m) = \underbrace{\left(\overline{v'^2 - u'^2}, -\overline{u'v'}\right)}_{\text{Eddy part}} \cdot \underbrace{\left(\frac{\partial \overline{u}}{\partial x} - \overline{v}\frac{\tan\phi}{r_e}, \frac{\partial \overline{u}}{\partial y} + \frac{\partial \overline{v}}{\partial x} + \overline{u}\frac{\tan\phi}{r_e}\right)}_{\text{Mean part}}, \tag{3}$$

where $C(P_e, P_m)$ and $C(K_e, K_m)$ are the conversion between the eddy and mean potential and kinetic energy, respectively, u and v are the zonal and meridional components of the wind, respectively, g is the gravitational constant, f is the Coriolis parameter, ρ is the density of air, T is temperature, r_e is the radius of Earth and $\overline{N}$ is the Brunt-Väisälä frequency:

$$\overline{N} = \sqrt{-\frac{\rho g^2}{\overline{\theta}}\frac{\partial \overline{\theta}}{\partial p}}, \tag{4}$$

where p is the pressure, and θ is the potential temperature. Overbar and prime represent mean and deviation from a mean. In this study, the mean is defined as a low pass from 30 days, which is much longer than the timescale of the storms (about 2–7 days). Additionally, to focus on large-scale mean flow patterns, a lowpass from wavenumber 5 was used. Eddy terms are not studied in this research directly, only through the Lagrangian growth properties.

Next, the mean flow quantities used for regression against individual storm growth are constructed based on the mean-dependent component of the conversion rates (right brace in Equations 2 and 3).

$$\left(\widehat{\mathrm{CP}}_x, \widehat{\mathrm{CP}}_y\right) = \frac{f}{\overline{N}}\left(\frac{\partial \overline{v}}{\partial z}, \frac{\partial \overline{u}}{\partial z}\right), \tag{5}$$

$$\left(\widehat{\mathrm{CK}}_x, \widehat{\mathrm{CK}}_y\right) = \left(\frac{\partial \overline{u}}{\partial x} - \overline{v}\frac{\tan\phi}{r_e}, \frac{\partial \overline{u}}{\partial y} + \frac{\partial \overline{v}}{\partial x} + \overline{u}\frac{\tan\phi}{r_e}\right), \tag{6}$$

These mean components are measured in rate units (day^{-1}) and will therefore be referred to in the plural as shear rates. The baroclinic shear rates are mainly proportional to the vertical shear of the winds, while barotropic shear rates are mainly proportional to the horizontal shear of the winds. The shear rates can be interpreted as the barotropic and baroclinic energy conversion rates for a given storm energy, as the eddy part is proportional to the anomalies squared, similar to EKE.

To simplify the baroclinic components of the shear rate, constant stratification, and wind shear are assumed, eliminating variability in the vertical dimension. Additionally, the mean wind component is assumed to vanish at the surface, as surface winds are generally weak and poorly captured by the ERA-5 reanalysis (Belmonte Rivas & Stoffelen, 2019). The resulting estimate for the baroclinic part is:

$$\left(\widehat{\mathrm{CP}}_x, \widehat{\mathrm{CP}}_y\right) = \frac{f}{\overline{N}H_{300}}\left(\overline{v}_{300}, \overline{u}_{300}\right), \tag{7}$$

where subscript denotes the pressure level that is used. N is estimated as:

$$\overline{N} = \sqrt{-\frac{\rho_{500} g^2}{\overline{\theta}_{500}} \frac{\overline{\theta}_{300} - \overline{\theta}_{850}}{p_{300} - p_{850}}}, \tag{8}$$

where ρ is calculated based on the ideal gas law. The magnitude of the baroclinic shear rate vector is used to define the baroclinicity:

$$\mathrm{BC} \equiv \frac{f}{\overline{N} H_{300}} \sqrt{\overline{v}_{300}^2 + \overline{u}_{300}^2}. \tag{9}$$

This definition of baroclinicity is closely related to the Eady Growth Rate (Eady, 1949), which represents the linear baroclinic instability prediction for the growth rate of anomalies and is widely used in Eulerian studies to analyze storm activity responses (e.g., Lehmann et al., 2014).

To simplify the barotropic shear rates, we consider that barotropic conversion primarily occurs in the upper atmosphere (Peixóto & Oort, 1992). Therefore, the mean flow at 300 hPa is used to assess the barotropic component of the shear rate:

$$\left(\widehat{\mathrm{CK}}_x, \widehat{\mathrm{CK}}_y\right) = \left(\frac{\partial \overline{u}_{300}}{\partial x} - \overline{v}_{300} \frac{\tan\phi}{r_e}, \frac{\partial \overline{u}_{300}}{\partial y} + \frac{\partial \overline{v}_{300}}{\partial x} + \overline{u}_{300} \frac{\tan\phi}{r_e}\right), \tag{10}$$

where $\widehat{\mathrm{CK}}_x$ and $\widehat{\mathrm{CK}}_y$ are known as stretching deformation and shearing deformation, respectively (Mak & Cai, 1989).

For individual storms, additional energy sources may play a significant role, such as ageostrophic energy fluxes (e.g., Orlanski & Katzfey, 1991) and diabatic heating (e.g., Weijenborg & Spengler, 2020). These sources could indirectly influence our analysis. For example, diabatic heating is crucial in maintaining the baroclinic structure of the atmosphere (Papritz & Spengler, 2015). Therefore, future work should aim to quantify the specific physical mechanisms underlying the observed relationships, including the contribution of diabatic heating.

3. The Lagrangian Response to Baroclinicity

3.1. The Empirical Relation Between Growth and Baroclinicity

The study first examines how storm growth responds to the baroclinic characteristics of the mean flow (baroclinicity), a key driver of storm development. This is achieved by calculating the baroclinicity (BC, Equation 9) experienced by storms, averaged both spatially within a composite box and temporally from genesis to MI (Section 2.2). Storms are then classified based on their average BC using a K-means algorithm (Pedregosa et al., 2011), which optimally partitions them into clusters. The average growth properties (e.g., MI) are then plotted against the mean BC for each cluster. By averaging storms that experienced similar BC, the analysis statistically removes variability due to uncorrelated factors, such as synoptic conditions of the eddy fields, effectively isolating the impact of baroclinicity on individual storm growth.

First, the connection between BC and the MI (Equation 1) of the cyclones is examined (Figure 2). For values of BC lower than 2.5 day^{-1}, the MI is positively correlated to BC (correlation of 0.96). This finding aligns with our expectation that regions of enhanced baroclinicity, such as the storm tracks, would be associated with increased storm activity. However, the positive correlation breaks at high BC. Indeed, calculating the correlation only for BC values larger than 2.5 day^{-1} results in a correlation of −0.37. This non-monotonic behavior might play a significant role in the dynamics of regions characterized by extreme baroclinicity, such as the Pacific during midwinter (Nakamura, 1992). This explains why the cyclonic contribution to EKE saturates during midwinter (Okajima et al., 2023) even though the track density peaks during midwinter (Okajima et al., 2021). For anticyclones, the MI increase rate slows down at high baroclinicity (0.95 and 0.80 correlation for values below and above 2.5 day^{-1} respectively, Figure 2d).

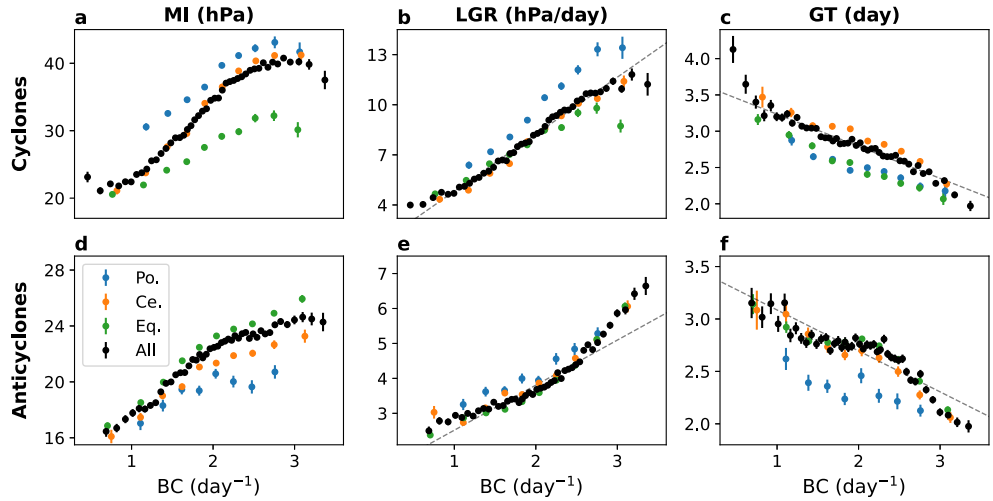

Figure 2. The relation of cyclones' (a) MI (hPa), (b) LGR (hPa·day^{-1}), and (c) GT (day), to the composite mean BC (day^{-1}) for (black) all cyclones, (blue) cyclones poleward of the jet core, (orange) around the center of the jet core, and (green) equatorward of the jet core. The dashed curve in (b, c, e, f) is the linear regression between the BC and the Lagrangian properties. The parameters of the fit appear in Table S1 of Supporting Information S1. (d–f) Same as (a–c), but for anticyclones. Fitted parameters for anticyclones appear in Table S2 of Supporting Information S1. Error bars represent the standard error within the BC clusters. Only clusters that have more than 100 storms are plotted. Poleward, around the center, and equatorward of the jet are defined as cyclones (anticyclones) that experienced meridional shear of zonal wind lower than −0.75 (−0.5), between −0.1 (−0.15) and 0.1 (0.15) and higher than 0.75 (0.5) (day^{-1}), respectively. Wider margins of shear are used for anticyclones because they are fewer. The black dots reach higher BC values as including storms from all parts of the jet increases the maximum BC at which 100 storms are obtained.

Dividing storms into equatorward, central, and poleward jet regions (Figure 2a; blue, orange, and green dots, respectively) reveals that cyclones are strongest on the poleward side of the jet and weakest on the equatorward side, while anticyclones exhibit the opposite trend.

To explain the non-monotonic behavior of the MI-BC relation, the MI is decomposed into GT and LGR, defined as the actual average rate of intensification during the growth stage, as measured by the tracking algorithm:

$$\mathrm{MI}_{\mathrm{cyclones}} \approx \mathrm{LGR} \times \mathrm{GT}, \tag{11}$$

where the approximation becomes exact when the initial intensity is fixed.

The LGR monotonically increases with BC for all values (0.96 for both cyclones and anticyclones Figures 2b and 2e). Since BC closely resembles the prediction for the baroclinic growth rate in linear instability models (e.g., Charney, 1947; Eady, 1949; Phillips, 1954), its linear relationship with LGR suggests that these models accurately capture the average cyclone growth.

However, the GT is negatively correlated with BC (correlation of −0.96 and −0.92 for cyclones and anticyclones, respectively, Figures 2c and 2f), indicating that the reduction in GT is responsible for the decrease in MI at high BC values. The reduction in GT with increasing baroclinicity aligns with previous meteorological studies of the West Pacific (Schemm et al., 2021), which showed that GT reduces from summer to winter, opposing the seasonal trend in baroclinicity. This trend was also observed in idealized GCM simulations, which demonstrated that it stemmed from the mean state's influence on the vertical structure of baroclinic waves (Hadas & Kaspi, 2021).

Decomposing the contribution from different regions relative to the jet shows that cyclones on the poleward side of the jet have a higher LGR (Figure 2b, blue vs. green and orange), consistent with their larger MI. In addition, cyclones on the center of the jet have a higher GT (Figure 2c, orange vs. green and blue), which is consistent with their greater MI compared to cyclones on the equatorward side of the jet. Anticyclones on the poleward side of the jet have slightly higher LGR and much lower GT, such that their MI is lower (Figures 2d–2f, blue vs. orange and green).

The observed LGR and GT trends indicate that the increase in MI at most BC values can be attributed to the increase in LGR, while the decline at high BC is driven by the decrease in GT. To quantify the inherent nonlinearity arising from the competing effects of LGR and GT, a linear model is applied to relate LGR and GT to BC (Figures 2b, 2c, 2e and 2f solid, the coefficients for cyclones and anticyclones are given in Tables S1 and S2 of Supporting Information S1, respectively). The constant coefficients for LGR are small (for the range of BC relevant to Earth), which fits our expectation that no baroclinicity will result in no growth. The main difference in the coefficients between cyclones and anticyclones is that the linear coefficient for the LGR is about three times larger for cyclones. In contrast, the fitted coefficients for the GT are remarkably similar.

Using the fitted coefficients, the MI is approximated as the multiplication of the two curves, which results in a parabola. The resulting estimate for MI is given by:

$$\mathrm{MI}_{\mathrm{cyclones}} \approx 12.0\mathrm{BC} - 1.4\mathrm{BC}^2, \tag{12}$$

$$\mathrm{MI}_{\mathrm{anticyclones}} \approx 4.4\mathrm{BC} - 0.48\mathrm{BC}^2, \tag{13}$$

where the constant term is neglected because it is small. The units of the linear and quadratic coefficients are hPa·day and hPa·day^2, respectively. The first term can be interpreted as the linear increase in MI due to the increase in LGR, while the second term can be interpreted as the nonlinear decrease in MI due to the decrease in GT. For low and medium values of BC (1 day^{-1}), the linear term contributes about nine times more than the nonlinear term, while for high BC (2.5 day^{-1}), it contributes only about three times more. This demonstrates why the linear approximation works well for most values of baroclinicity relevant to Earth's climate, but breaks down for high baroclinicity values.

These findings highlight the value of the Lagrangian perspective in studying mean-eddy interactions by resolving the complexities of individual storm growth. The results show that MI, which is expected to correlate with Eulerian EKE (Schemm & Schneider, 2018), increases monotonically with BC at low and medium baroclinicity levels, but decreases for cyclones and saturates for anticyclones at higher values. The LGR increases monotonically with baroclinicity, aligning with predictions from linear baroclinic instability models. However, the observed non-monotonic behavior at high baroclinicity arises due to a reduction in GT. Additionally, we find a significant difference in the growth rates of different baroclinic wave phases, with cyclones exhibiting much faster growth. Finally, the location relative to the jet (which affects the barotropic shear) influences the growth of individual cyclones and anticyclones, a topic further explored in Section 4.

3.2. Theoretical View on the Empirical Response

To identify a potential physical mechanism underlying the nonlinear behavior of MI, the increase in LGR, and the reduction in GT with baroclinicity, this section constructs a minimal idealized model that reproduces the observed trends (Section 3.1). To build intuition, we first consider an overly simplified model. Following Davies and Bishop (1994) and using linear theory, the time evolution of two counter-propagating Rossby waves with common amplitude A, and a relative phase of ϵ in a zonal flow with shear Λ, Brunt-Väisälä frequency N and Coriolis parameter f (characterized by BC$=\frac{\Lambda f}{N}$), is given by:

$$\frac{\partial A}{\partial t} = -\mathrm{BC}\sin(\epsilon)A\Delta, \tag{14}$$

$$\frac{\partial \epsilon}{\partial t} = \mathrm{BC}(\alpha - \cos(\epsilon))\,2\Delta, \tag{15}$$

where α is a geometric factor proportional to the ratio between the disturbance length scale and the Rossby radius of deformation (typically slightly smaller than 1 for cyclones), and Δ is a geometric factor related to zonal and meridional length scales (typically close to 1).

These equations indicate that wave growth requires a phase shift between 0 and $-\pi$ and that the rate of phase change depends on baroclinicity. Dividing both sides by BC allows reformulation in terms of normalized time

$\left(\frac{\partial}{\partial t \cdot \mathrm{BC}}\right)$. From this perspective, higher baroclinicity shortens the timescale, accelerating both growth rate and phase change, which can reduce GT (Badger & Hoskins, 2001; Davies & Bishop, 1994; Tamarin et al., 2015).

Supporting this idea, Hadas and Kaspi (2021) used an aquaplanet GCM to show that shorter GT with increasing baroclinicity results from faster upper-level eddy drift, driven by a stronger jet stream. Similarly, Schemm and Rivière (2019) found that meridional and zonal tilt contribute to storm suppression during the Pacific midwinter minimum. Thus, we hypothesize that the influence of baroclinicity on phase evolution drives the observed reduction in GT and the resulting nonlinear trend of MI in the empirical results.

However, the linear dynamics of these equations are not characterized by an MI or GT, as the normal mode solution has a constant phase (ϵ) and indefinitely growing amplitude (A), a typical limitation of linear models. Therefore, a more complex model is required to test our hypothesis. To introduce greater complexity and establish a connection to the energetic perspective, we construct a framework based on the Lorenz energy cycle (e.g., Lorenz, 1955; Oort & Peixóto, 1983):

$$\frac{\partial P_e}{\partial t} = \mathrm{CP} + \underbrace{\frac{1}{\rho\bar{T}}\omega' T'}_{\mathrm{CE}}, \tag{16}$$

$$\frac{\partial K_e}{\partial t} = -\mathrm{CK} - \underbrace{\frac{1}{\rho\bar{T}}\omega' T'}_{\mathrm{CE}}, \tag{17}$$

where $P_e = \frac{1}{2}\left(\frac{gT'}{\bar{T}N}\right)^2$ and $K_e = \frac{1}{2}\left(u'^2 + v'^2\right)$ are the eddy available potential energy and kinetic energy, ω' is the vertical velocity anomaly, and CP and CK are the baroclinic and barotropic conversion (given by Equations 2 and 3, respectively). The last term in both equations is the conversion of P_e to K_e (CE). Assuming for simplicity that:

$$\begin{aligned} u', v' &\sim \sqrt{K_e}, \\ T', \omega' &\sim \sqrt{P_e}, \end{aligned} \tag{18}$$

where ω' is assumed to scale like the eddy potential energy as convection will be triggered by temperature anomalies created by baroclinic conversion at lower levels. Therefore, the eddy part of the conversion terms can be written as:

$$\begin{aligned} \mathrm{CK}_{\mathrm{eddy}} &\sim K_e, \\ \mathrm{CP}_{\mathrm{eddy}} &\sim \sqrt{K_e \cdot P_e}, \\ \mathrm{CE}_{\mathrm{eddy}} &\sim P_e, \end{aligned} \tag{19}$$

and then Equations 16 and 17 can be expressed as:

$$\frac{\partial P_e}{\partial t} = \underbrace{b\sqrt{K_e \cdot P_e}}_{\mathrm{CP}} - \underbrace{cP_e}_{\mathrm{CE}}, \tag{20}$$

$$\frac{\partial K_e}{\partial t} = -\underbrace{aK_e}_{\mathrm{CK}} + \underbrace{cP_e}_{\mathrm{CE}}, \tag{21}$$

Where the coefficients a, b, c have units of rate and incorporate in them two crucial properties: the correlation between the eddy terms and the dependence on the mean flow conditions.

Next, the competing effects of baroclinicity on phase and amplitude evolution in the linear model (Equations 14 and 15) is incorporated into the more complex model (Equations 16 and 17). In the real atmosphere, storm growth depends on the phase between the upper and lower part of the storms, as westerly tilted anomalies create a positive correlation between lower-level temperature and wind perturbations, which is essential for baroclinic energy

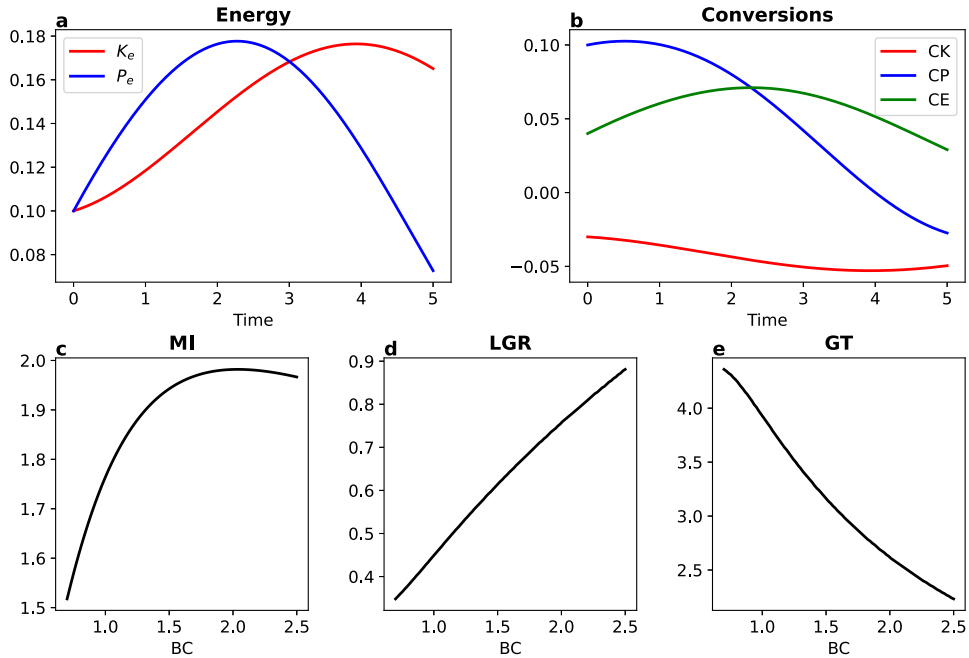

Figure 3. (a) The solution of Equations 20 and 21 for $a = 0.4$, BC $= 1$, $c = 0.4$, $\tau = 4$ with initial perturbations $P_e(0) = 0.1$, $K_e(0) = 0.1$ as a function of time. (b) The contribution of (blue) baroclinic conversion (CP), (green) conversion of K_e to P_e (CE), and (red) barotropic conversion (CK) to the energy budget as a function of time. (c) The MI (defined as the maximum of K_e), (d) the LGR (defined as the average rate of change of K_e) and (e) the GT (defined as the time step of maximum K_e) for a range of BC values, with a, c, and τ fixed to the values used in (a and b).

conversion from the mean flow to the eddies (Equation 2, Hoskins & James, 2014). Thus, the indirect effect of baroclinicity on storm growth—through its influence on phase evolution (ϵ), can be incorporated in a simplified way by modifying the efficiency of baroclinic conversion as a function of time:

$$b(t) = \mathrm{BC}(1 - \mathrm{BC} \cdot t/\tau), \tag{22}$$

where τ is a non-dimensional parameter that sets the relation between the BC and the rate of change in ϵ. The overall factor BC captures the idea that stronger baroclinicity increases the potential rate of energy extraction from the mean flow. Meanwhile, the $(1 - \mathrm{BC} \cdot t/\tau)$ term reflects how phase evolution reduces the efficiency of baroclinic conversion over time. Comparing Equations 14 and 22, the time dependence can be interpreted as an upper-level wave that starts with an initial phase of $-\frac{\pi}{2}$, and its phase evolves over time in such a way that the efficiency of baroclinic conversion decreases linearly with time.

To demonstrate the relevance of this equation to the idealized lifecycle of storms, Equations 20 and 21 are integrated over time, starting from a westward tilted with height small anomaly. Using $a = 0.4$, BC $= 1$, $c = 0.4$, $\tau = 4$, results in a realistic idealized energy lifecycle (Simmons & Hoskins, 1978): Initially, P_e increases (Figure 3a blue) due to CP (Figure 3b blue). Then, as the phase decreases, CE surpasses CP (Figure 3b blue vs. green), causing P_e to decline while K_e increases (Figure 3a blue and red). Finally, as P_e reduces, the CK exceeds CE (Figure 3b red vs. green), ending the K_e growth.

Sensitivity tests on BC reveal a trend similar to that in Section 3.1. An analog to MI can be constructed as the maximum of K_e. Solving the equations for a range of BC values (holding a, c, τ constant) results in an increase in MI for small BC values and saturation or even decrease for high BC values (Figure 3c). To further analyze this behavior, MI is decomposed into GT and LGR, where LGR is defined as the average growth rate during the increase in K_e and GT is the time at which K_e reaches its maximum. This decomposition reveals that while LGR consistently increases across the entire BC range (Figure 3d), GT decreases (Figure 3e), aligns with the trends presented in Section 3.1.

The results demonstrate that an idealized model based on the Lorenz energy cycle successfully reproduces the observed trends of MI, LGR, and GT with baroclinicity (Section 3.1) when incorporating a coupling between baroclinicity and the rate of change in baroclinic conversion efficiency. This suggests that the shorter GT and nonlinear decrease in MI can be attributed to a faster decline in baroclinic conversion efficiency with increasing baroclinicity, driven by accelerated phase changes between upper- and lower-level waves. These phase changes are induced by the strong vertical wind shear characteristic of high baroclinicity. Future studies should extend the model to include nonlinear effects, such as phase locking of baroclinic waves and its disruption by cascades and interactions with shorter waves (Tamarin et al., 2015), and diabatic effects such as latent cooling and surface fluxes (Haualand & Spengler, 2019, 2020), which might explain the deviations of the empirically found trends from the results of the idealized model.

4. The Lagrangian Response to the Full Atmospheric Mean State

Although barotropic properties of the mean flow are known to have a profound influence on the dynamics of storms (Chemke et al., 2022; James, 1987; Lorenz, 1955; Rivière et al., 2013), which is supported by the difference in growth between storms in different locations relative to the jet (Figure 2), they are rarely considered when assessing the storm track response to climatic forcing. Therefore, in this section, the influence of the barotropic shear of the mean flow on storm growth is systematically studied, and compared to the influence of the baroclinic properties.

The shear rates (Section 2.3) quantify the barotropic and baroclinic properties of the mean flow. Barotropic properties are measured using $\widehat{\mathrm{CK}}_x$, and $\widehat{\mathrm{CK}}_y$, which are proportional to horizontal shear (Equation 10), while baroclinic properties are quantified by $\widehat{\mathrm{CP}}_x$, and $\widehat{\mathrm{CP}}_y$, which are proportional to vertical shear (Equation 7). The response of storms' growth to each shear component is analyzed by sorting cyclones and anticyclones based on the composite and temporal average shear rates during their growth stage and examining the resulting differences in LGR and GT (Section 2.2). Additionally, a 4-dimensional linear model is fitted to quantify the relative importance of each shear rate term (see Section S1 in Supporting Information S1).

The discussion begins by examining the frequency at which storms experience different conversion rates. It then explores the influence of shear rates on LGR, which is identified as the most complex aspect, following a structured approach. First, the effect of baroclinic characteristics on cyclones is analyzed, followed by an investigation of the barotropic characteristics. This is then extended to assess the relative importance of baroclinic versus barotropic properties before comparing the differences between cyclones and anticyclones. After addressing these aspects, the impact on GT is analyzed. Finally, the findings are synthesized into a comprehensive summary of how baroclinic and barotropic properties influence storm growth.

First, the distribution of cyclones and anticyclones in the shear rate space ($\widehat{\mathrm{CP}}_x$, $\widehat{\mathrm{CP}}_y$, $\widehat{\mathrm{CK}}_x$, $\widehat{\mathrm{CK}}_y$) is analyzed. The shear rate coefficients generally exhibit low correlation (Tables S3 and S4 of Supporting Information S1) and are therefore treated as independent variables. Storms typically experience positive values of $\widehat{\mathrm{CP}}_y$, indicating easterly jets, which are characteristic of storm development regions (e.g., Chang et al., 2002). The other coefficients are centered around zero, with both positive and negative values observed. The key distributional difference between cyclones and anticyclones is that anticyclones experience higher values of $\widehat{\mathrm{CK}}_y$, meaning they are more frequently located on the anticyclonic (equatorward) side of the jet. This aligns with previous findings showing that anticyclone tracks are, on average, more equatorward (Hoskins & Hodges, 2002, 2005).

The effect of the baroclinic terms on cyclones' LGR (Figure 4b) shows a positive correlation with $\widehat{\mathrm{CP}}_y$ and the absolute value of $\widehat{\mathrm{CP}}_x$. This result aligns with findings from Section 3.1 and previous studies showing a strong connection between high growth rates and high baroclinicity (e.g., Hoskins & Hodges, 2002). A linear model indicates that, given the fitted coefficients and the relevant value range, $\widehat{\mathrm{CP}}_y$ has three times the impact of $\widehat{\mathrm{CP}}_x$.

Cyclones' LGR is negatively correlated with both barotropic shear rates (Figure 4e). Linear Regression analysis shows that $\widehat{\mathrm{CK}}_x$ and $\widehat{\mathrm{CK}}_y$ have similar contribution. The negative correlation between $\widehat{\mathrm{CK}}_y$ and LGR fits the results in Figure 2b, as cyclones on the poleward side of the jet exhibit lower $\widehat{\mathrm{CK}}_y$ and higher LGR, while the opposite holds for cyclones on the equatorward side. Furthermore, the high LGR at negative values of both $\widehat{\mathrm{CK}}_y$

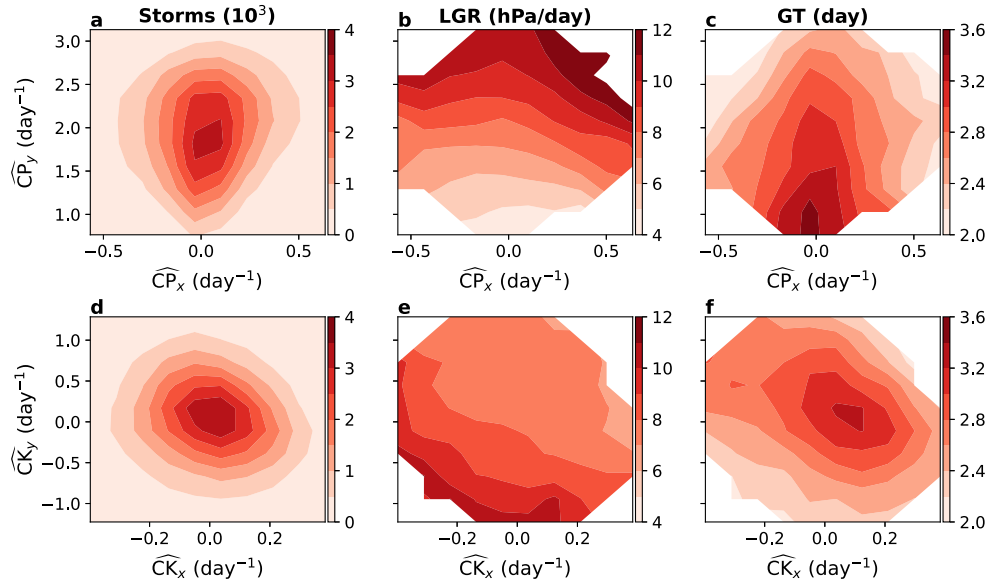

Figure 4. (a, d) The Number of storms, (b, e) LGR (hPa·day^{-1}), and (c, f) GT (days) as a function of (a–c) $\widehat{CP}_x$ and $\widehat{CP}_y$ (day^{-1}), and (d–f) $\widehat{CK}_x$ and $\widehat{CK}_y$ (day^{-1}).

and $\widehat{CK}_x$ is consistent with expectations that storms on the poleward side of the jet exit region experience enhanced cyclonic growth, driven by ageostrophic wind divergence at high levels (Martin, 2013).

Comparing the contribution of the barotropic and baroclinic shear rates to cyclones' LGR (Figure 4b vs. Figure 4e) reveals that the baroclinic contribution is approximately twice as large. For anticyclones, the barotropic influence on LGR is small, being about four times smaller than the baroclinic contribution (Figure 5b vs. Figure 5e). Additionally, linear analysis indicates that $\widehat{CP}_y$ is roughly twice as influential as $\widehat{CP}_x$.

The GT of both cyclones and anticyclones responds similarly to the barotropic and baroclinic properties of the mean flow, decreasing with increasing shear rates (Figures 4c, 4f, 5c, and 5f), at a comparable rate. Additionally, all four conversion rates appear to influence GT similarly. This pattern aligns with the observation that cyclones

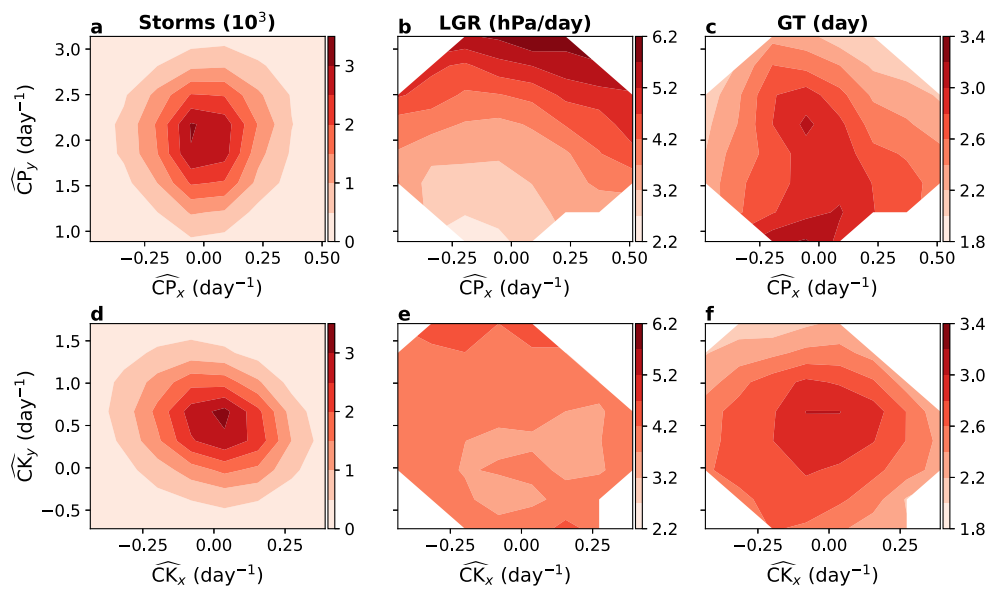

Figure 5. Same as Figure 4, but for anticyclones.

both poleward and equatorward of the jet exhibit shorter GT than those near the jet core (Figure 2c orange vs. green and blue).

A key difference between cyclones and anticyclones is the optimal $\widehat{\mathrm{CK}}_y$ for GT, which is about 0.5 day^{-1} for anticyclones, compared to about 0.1 for cyclones (Figure 4f vs. Figure 5f). This aligns with the observation that poleward anticyclones have much lower GT, while those near the jet core and equatorward of the jet exhibit similar GT values (Figure 2f orange vs. green). Since very high values of $\widehat{\mathrm{CK}}_y$ are rare (Figure 5d), this may explain the observed distribution. A possible explanation for the longer GT of equatorward cyclones and anticyclones is that some storms in this region may initially form as thermal lows, which later transition into baroclinic storms (Campins et al., 2000), extending their overall GT.

Building on Section 3.1, this analysis reveals key details about the mean flow's impact on storm growth. For LGR, baroclinic properties play a larger role for cyclones and dominate for anticyclones, while the mean zonal flow has a stronger influence than the meridional flow. In contrast, GT is equally affected by baroclinic and barotropic properties, as well as by zonal and meridional winds. An extension of the mechanism proposed in Section 3.2 could be suggested to explain this trend: the horizontal and vertical shear of the flow disrupt the baroclinic structure necessary for growth through differential advection. Consequently, stronger shear, characterized by higher baroclinic and barotropic shear rates, leads to a reduction in the growth time of the wave. This generalization of the mechanism fits previous results of Schemm and Rivière (2019), which showed over the Pacific during midwinter that meridional tilt has a similar effect on baroclinic conversion to zonal shear. Further research, which includes diabatic effects, is needed to fully understand the underlying mechanism.

5. Summary

When investigating the midlatitude climate's response to changes in atmospheric forcing, whether natural or anthropogenic, a key challenge lies in understanding how eddies respond to the mean state of the atmosphere. While many studies have explored this interaction from an Eulerian perspective, there has yet to be a systematic exploration of how the background state of the atmosphere impacts the growth of storms from a Lagrangian perspective. To address this gap, this study investigates the statistical relationship between commonly used baroclinic and barotropic properties of the background flow and the growth of individual cyclones and anticyclones.

A systematic quantification of the influence of baroclinicity (Equation 9), on Maximum Intensity (MI, Figures 2a and 2d) shows that MI generally increases with baroclinicity. However, at extreme baroclinicity values, this trend reverses for cyclones and significantly slows down for anticyclones. This behavior is particularly relevant to midlatitude weather responses to extreme baroclinicity, such as those observed over the North Pacific during midwinter.

To explain this nonlinearity, MI is decomposed into Lagrangian Growth Rate (LGR) and Growth Time (GT). LGR increases monotonically with baroclinicity (Figures 2b and 2e), confirming that the growth rate predicted by linear baroclinic instability models aligns with observed Lagrangian growth. However, GT decreases with baroclinicity (Figures 2c and 2f), indicating that the linear increase in MI at most baroclinicity values is driven by the rapid rise in LGR, while the MI decline at extreme baroclinicity for cyclones results from nonlinear effects due to GT reduction. Based on these empirical results, the magnitudes of the linear and nonlinear terms are estimated, leading to a nonlinear correction to the classical relationship between baroclinicity and storms' activity (Equations 12 and 13).

The observed relationship between baroclinicity, MI, LGR, and GT is successfully reproduced (Figure 3) using a simple growth model based on the Lorenz energy cycle, where the rate of change in baroclinic conversion efficiency is coupled to baroclinicity (Equations 21 and 22). This demonstrates that the reduction in GT and the nonlinear decrease in MI can arise from a faster decline in baroclinic conversion efficiency with increasing baroclinicity, which is intuitively linked to phase shifts between the upper- and lower-level waves. In reality, this coupling results from faster differential advection of the upper-level wave relative to the lower-level wave, driven by enhanced vertical shear of the mean flow under higher baroclinicity conditions.

Incorporating the barotropic properties of the mean flow (horizontal shear) into the analysis reveals that they have a weaker influence on LGR, being twice less influential for cyclones and four times less influential for

anticyclones (Figure 4b vs. Figures 4e and 5b vs. Figure 5e). However, GT for both cyclones and anticyclones is strongly affected by both barotropic and baroclinic characteristics of the mean flow (Figures 4c, 4f, 5c and 5f).

The complex dynamics revealed by this study underscore the importance of considering the response of individual storms to climatic changes. The findings demonstrate that the commonly assumed linear relationship between storm activity and mean baroclinicity holds only at low baroclinicity levels, highlighting the need for caution when applying it to high-baroclinicity regions. However, they also show that idealized dry models effectively capture key aspects of the observed trends. Furthermore, the results underscore the importance of accounting for both barotropic and baroclinic properties of the mean flow when using eddy–mean flow frameworks to study storm track responses to climatic conditions.

These findings raise several fundamental open questions. A key unresolved issue is the relative importance of mean flow versus eddy flow in individual storm growth, which is critical for the assessment of storms' internal variability for attribution efforts. Another crucial question is the physical mechanism underlying the observed trends, particularly the reduction in GT with barotropic properties, and the role of processes such as diabatic heating in this relationship. Additionally, this study focuses on how the mean flow influences storms, but the reverse interaction—how storms feedback onto the mean flow—remains unexplored. Future research should address this feedback to develop a comprehensive understanding of eddy-mean flow interactions.

Appendix A: Baroclinic and Barotropic Energy Conversion

To obtain the equation for barotropic conversion, Equation 4 in Simmons et al. (1983) is multiplied by *rho* to translate into units of energy per volume:

$$C(K_e, K_m) = \rho\left(\overline{v'^2 - u'^2},\ -\overline{u'v'}\right) \cdot \left(\frac{\partial \overline{u}}{\partial x} - \overline{v}\frac{\tan\phi}{r_e},\ \cos\phi\,\frac{\partial}{\partial y}\left(\frac{\overline{u}}{\cos\phi}\right) + \frac{\partial \overline{v}}{\partial x}\right) \underbrace{\rightarrow}_{\frac{\partial}{\partial y} = \frac{1}{r_e}\frac{\partial}{\partial \phi}} \tag{A1}$$

$$= \rho\left(\overline{v'^2 - u'^2},\ -\overline{u'v'}\right) \cdot \left(\frac{\partial \overline{u}}{\partial x} - \overline{v}\frac{\tan\phi}{r_e},\ \frac{\partial \overline{u}}{\partial y} + \frac{\partial \overline{v}}{\partial x} + \overline{u}\frac{\tan\phi}{r_e}\right). \tag{A2}$$

To obtain the equation for baroclinic conversion, we multiply the second term in the right-hand-side of Equation 4.2 in Orlanski and Katzfey (1991) with ρ:

$$C(P_e, P_m) = \frac{1}{\overline{\theta}\frac{\partial \overline{\theta}}{\partial p}}\left(\overline{u'\theta'}, \overline{v'\theta'}\right) \cdot \left(\frac{\partial \overline{\theta}}{\partial x}, \frac{\partial \overline{\theta}}{\partial y}\right). \tag{A3}$$

Next, thermal wind balance is used to translate the gradient of potential temperature to wind shear. Furthermore, we cancel the Exner function between the $\overline{\theta}$ and θ' terms in the left part of the dot product. Finally, we express the mean potential temperature vertical gradient in terms of the Brunt–Väisälä frequency ($\bar{N}$) using Equation 4. This leads to the final version presented in the main text:

$$C(P_e, P_m) = \frac{\rho g}{\overline{N}\overline{T}}\left(\overline{u'T'}, \overline{v'T'}\right) \cdot \frac{f}{\overline{N}}\left(\frac{\partial \overline{v}}{\partial z}, \frac{\partial \overline{u}}{\partial z}\right). \tag{A4}$$

Conflict of Interest

The authors declare no conflicts of interest relevant to this study.

Data Availability Statement

No new data sets were generated during the current study. The three-dimensional atmospheric variables on pressure levels (e.g., zonal and meridional wind) are available from Copernicus through the data set "ERA-5 hourly data on pressure levels from 1940 to present" Hersbach et al. (2023a). Sea level pressure data is available from Copernicus through the data set "ERA-5 hourly data on single levels from 1940 to present" Hersbach et al. (2023b).

Acknowledgments
This research has been supported by the Azrieli fellowship and the Israeli Science Foundation (Grant 996/20).

References

Badger, J., & Hoskins, B. (2001). Simple initial value problems and mechanisms for baroclinic growth. *Journal of the Atmospheric Sciences*, *58*(1), 38–49. https://doi.org/10.1175/1520-0469(2001)058<0038:sivpam>2.0.co;2

Belmonte Rivas, M., & Stoffelen, A. (2019). Characterizing ERA-Interim and ERA5 surface wind biases using ASCAT. *Ocean Science*, *15*(3), 831–852. https://doi.org/10.5194/os-15-831-2019

Campins, J., Genovés, A., Jansa, A., Guijarro, J., & Ramis, C. (2000). A catalogue and a classification of surface cyclones for the western mediterranean. *International Journal of Climatology*, *20*(9), 969–984. https://doi.org/10.1002/1097-0088(200007)20:9<969::aid-joc519>3.3.co;2-w

Chang, E. K. M., Lee, S., & Swanson, K. L. (2002). Storm track dynamics. *Journal of Climate*, *15*(16), 2163–2183. https://doi.org/10.1175/1520-0442(2002)015<02163:std>2.0.co;2

Charney, J. G. (1947). The dynamics of long waves in a baroclinic westerly current. *Journal of Meteorology*, *4*(5), 136–162. https://doi.org/10.1175/1520-0469(1947)004<0136:tdolwi>2.0.co;2

Chemke, R., Ming, Y., & Yuval, J. (2022). The intensification of winter mid-latitude storm tracks in the southern hemisphere. *Nature Cliamte Change*, *12*(6), 553–557. https://doi.org/10.1038/s41558-022-01368-8

Davies, H., & Bishop, C. (1994). Eady edge waves and rapid development. *Journal of the Atmospheric Sciences*, *51*(13), 1930–1946. https://doi.org/10.1175/1520-0469(1994)051<1930:eeward>2.0.co;2

Davis, C. A., & Emanuel, K. A. (1991). Potential vorticity diagnostics of cyclogenesis. *Monthly Weather Review*, *119*(8), 1929–1953. https://doi.org/10.1175/1520-0493(1991)119<1929:pvdoc>2.0.co;2

Eady, E. T. (1949). Long waves and cyclone waves. *Tellus*, *1*(3), 33–52. https://doi.org/10.1111/j.2153-3490.1949.tb01265.x

Hadas, O., Datseris, G., Blanco, J., Bony, S., Caballero, R., Stevens, B., & Kaspi, Y. (2023). The role of baroclinic activity in controlling Earth's albedo in the present and future climates. *Proceedings of the National Academy of Sciences of the United States of America*, *120*(5), e2208778120. https://doi.org/10.1073/pnas.2208778120

Hadas, O., & Kaspi, Y. (2021). Suppression of baroclinic eddies by strong jets. *Journal of the Atmospheric Sciences*, *78*(8), 2445–2457.

Harnik, N., & Chang, E. K. M. (2004). The effects of variations in jet width on the growth of baroclinic waves: Implications for midwinter Pacific storm track variability. *Journal of the Atmospheric Sciences*, *61*(1), 23–40. https://doi.org/10.1175/1520-0469(2004)061<0023:teovij>2.0.co;2

Haualand, K. F., & Spengler, T. (2019). How does latent cooling affect baroclinic development in an idealized framework? *Journal of the Atmospheric Sciences*, *76*(9), 2701–2714. https://doi.org/10.1175/jas-d-18-0372.1

Haualand, K. F., & Spengler, T. (2020). Direct and indirect effects of surface fluxes on moist baroclinic development in an idealized framework. *Journal of the Atmospheric Sciences*, *77*(9), 3211–3225. https://doi.org/10.1175/jas-d-19-0328.1

Haualand, K. F., & Spengler, T. (2021). Relative importance of tropopause structure and diabatic heating for baroclinic instability. *Weath. and Climate Dyn*, *2*(3), 695–712. https://doi.org/10.5194/wcd-2-695-2021

Hersbach, H., Bell, B., Berrisford, P., Biavati, G., Horányi, A., Muñoz Sabater, J., et al. (2023a). Era5 hourly data on pressure levels from 1940 to present [Dataset]. *Copernicus Climate Change Service (C3S) Climate Data Store (CDS)*. https://doi.org/10.24381/cds.bd0915c6

Hersbach, H., Bell, B., Berrisford, P., Biavati, G., Horányi, A., Muñoz Sabater, J., et al. (2023b). Era5 hourly data on single levels from 1940 to present [Dataset]. *Copernicus Climate Change Service (C3S) Climate Data Store (CDS)*. https://doi.org/10.24381/cds.adbb2d47

Hersbach, H., Bell, B., Berrisford, P., Hirahara, S., Horányi, A., Muñoz-Sabater, J., et al. (2020). The ERA5 global reanalysis. *Quarterly Journal of the Royal Meteorological Society*, *146*(730), 1999–2049. https://doi.org/10.1002/qj.3803

Hodges, K. (1995). Feature tracking on the unit sphere. *Monthly Weather Review*, *123*(12), 3458–3465. https://doi.org/10.1175/1520-0493(1995)123<3458:ftotus>2.0.co;2

Hoskins, B., & Hodges, K. (2019). The annual cycle of northern hemisphere storm tracks. Part I: Seasons. *Journal of Climate*, *32*(6), 1743–1760. https://doi.org/10.1175/jcli-d-17-0870.1

Hoskins, B. J., & Hodges, K. I. (2002). New perspectives on the Northern hemisphere winter storm tracks. *Journal of the Atmospheric Sciences*, *59*(6), 1041–1061. https://doi.org/10.1175/1520-0469(2002)059<1041:npotnh>2.0.co;2

Hoskins, B. J., & Hodges, K. I. (2005). A new perspective on Southern Hemisphere storm tracks. *Journal of Climate*, *18*(20), 4108–4129. https://doi.org/10.1175/jcli3570.1

Hoskins, B. J., & James, I. N. (2014). *Fluid dynamics of the mid-latitude atmosphere*. John Wiley & Sons.

Hoskins, B. J., McIntyre, M. E., & Robertson, A. W. (1985). On the use and significance of isentropic potential vorticity maps. *Quarterly Journal of the Royal Meteorological Society*, *111*(470), 877–946. https://doi.org/10.1256/smsqj.47001

James, I. N. (1987). Suppression of baroclinic instability in horizontally sheared flows. *Journal of the Atmospheric Sciences*, *44*(24), 3710–3720. https://doi.org/10.1175/1520-0469(1987)044<3710:sobiih>2.0.co;2

Kang, J. M., Shaw, T. A., & Sun, L. (2024). Anthropogenic aerosols have significantly weakened the regional summertime circulation in the northern hemisphere during the satellite era. *AGU Adv*, *5*(6), e2024AV001318. https://doi.org/10.1029/2024av001318

Kang, J. M., & Son, S.-W. (2021). Development processes of the explosive cyclones over the Northwest Pacific: Potential vorticity tendency inversion. *Journal of the Atmospheric Sciences*, *78*(6), 1913–1930. https://doi.org/10.1175/jas-d-20-0151.1

Lehmann, J., Coumou, D., Frieler, K., Eliseev, A. V., & Levermann, A. (2014). Future changes in extratropical storm tracks and baroclinicity under climate change. *Environmental Research Letters*, *9*(8), 084002. https://doi.org/10.1088/1748-9326/9/8/084002

Lorenz, E. N. (1955). Available potential energy and the maintenance of the general circulation. *Tellus*, *7*(2), 157–167. https://doi.org/10.1111/j.2153-3490.1955.tb01148.x

Mak, M., & Cai, M. (1989). Local barotropic instability. *Journal of the Atmospheric Sciences*, *46*(21), 3289–3311. https://doi.org/10.1175/1520-0469(1989)046<3289:lbi>2.0.co;2

Martin, J. E. (2013). *Mid-latitude atmospheric dynamics: A first course*. Wiley.

Nakamura, H. (1992). Midwinter suppression of baroclinic wave activity in the Pacific. *Journal of the Atmospheric Sciences*, *49*(17), 1629–1642. https://doi.org/10.1175/1520-0469(1992)049<1629:msobwa>2.0.co;2

Nakamura, H., & Sampe, T. (2002). Trapping of synoptic-scale disturbances into the North-Pacific subtropical jet core in midwinter. *Geophysical Research Letters*, *29*(16), 8. https://doi.org/10.1029/2002gl015535

Nakamura, H., & Shimpo, A. (2004). Seasonal variations in the southern hemisphere storm tracks and jet streams as revealed in a reanalysis dataset. *Journal of Climate*, *17*(9), 1828–1844. https://doi.org/10.1175/1520-0442(2004)017<1828:svitsh>2.0.co;2

Okajima, S., Nakamura, H., & Kaspi, Y. (2021). Cyclonic and anticyclonic contributions to atmospheric energetics. *Scientific Reports*, *11*(1), 1–10. https://doi.org/10.1038/s41598-021-92548-7

Okajima, S., Nakamura, H., & Kaspi, Y. (2022). Energetics of transient eddies related to the midwinter minimum of the North Pacific storm-track activity. *Journal of Climate*, *35*(4), 1137–1156. https://doi.org/10.1175/jcli-d-21-0123.1

Okajima, S., Nakamura, H., & Kaspi, Y. (2023). Distinct roles of cyclones and anticyclones in setting the midwinter minimum of the North Pacific eddy activity: A Lagrangian perspective. *Journal of Climate*, *36*(14), 4793–4814. https://doi.org/10.1175/jcli-d-22-0474.1

Okajima, S., Nakamura, H., & Kaspi, Y. (2024). Anticyclonic suppression of the North Pacific transient eddy activity in midwinter. *Geophysical Research Letters*, *51*(2), e2023GL106932. https://doi.org/10.1029/2023gl106932

Oort, A. H., & Peixóto, J. P. (1983). Global angular momentum and energy balance requirements from observations. *Advances in Geophysics*, *25*, 355–490. https://doi.org/10.1016/s0065-2687(08)60177-6

Orlanski, I., & Chang, E. K. M. (1993). Ageostrophic geopotential fluxes in downstream and upstream development of baroclinic waves. *Journal of the Atmospheric Sciences*, *50*(2), 212–225. https://doi.org/10.1175/1520-0469(1993)050<0212:agfida>2.0.co;2

Orlanski, I., & Katzfey, J. (1991). The life cycle of a cyclone wave in the southern hemisphere. Part I: Eddy energy budget. *Journal of the Atmospheric Sciences*, *48*(17), 1972–1998. https://doi.org/10.1175/1520-0469(1991)048<1972:tlcoac>2.0.co;2

Papritz, L., & Spengler, T. (2015). Analysis of the slope of isentropic surfaces and its tendencies over the North Atlantic. *Quarterly Journal of the Royal Meteorological Society*, *141*(693), 3226–3238. https://doi.org/10.1002/qj.2605

Pedregosa, F., Varoquaux, G., Gramfort, A., Michel, V., Thirion, B., Grisel, O., et al. (2011). Scikit-learn: Machine learning in Python. *Journal of Machine Learning Research*, *12*, 2825–2830.

Peixóto, J. P., & Oort, A. H. (1974). The annual distribution of atmospheric energy on a planetary scale. *Journal of Geophysical Research*, *79*(15), 2149–2159. https://doi.org/10.1029/jc079i015p02149

Peixóto, J. P., & Oort, A. H. (1992). *Physics of climate*. AIP.

Phillips, N. A. (1954). Energy transformations and meridional circulations associated with simple baroclinic waves in a two level quasi-geostrophic model. *Telus*, *6*(3), 273–286. https://doi.org/10.1111/j.2153-3490.1954.tb01123.x

Rivière, G., Gilet, J.-B., & Oruba, L. (2013). Understanding the regeneration stage undergone by surface cyclones crossing a midlatitude jet in a two-layer model. *Journal of the Atmospheric Sciences*, *70*(9), 2832–2853. https://doi.org/10.1175/jas-d-12-0345.1

Rivière, G., & Joly, A. (2006). Role of the low-frequency deformation field on the explosive growth of extratropical cyclones at the jet exit. Part I: Barotropic critical region. *Journal of the Atmospheric Sciences*, *63*(8), 1965–1981. https://doi.org/10.1175/jas3728.1

Sanders, F., & Gyakum, J. R. (1980). Synoptic-dynamic climatology of the "bomb". *Monthly Weather Review*, *108*(10), 1589–1606. https://doi.org/10.1175/1520-0493(1980)108<1589:sdcot>2.0.co;2

Schemm, S., & Rivière, G. (2019). On the efficiency of baroclinic eddy growth and how it reduces the North Pacific storm-track intensity in midwinter. *Journal of Climate*, *32*(23), 8373–8398.

Schemm, S., & Schneider, T. (2018). Eddy lifetime, number, and diffusivity and the suppression of eddy kinetic energy in midwinter. *Journal of Climate*, *31*(14), 5649–5665. https://doi.org/10.1175/jcli-d-17-0644.1

Schemm, S., Wernli, H., & Binder, H. (2021). The storm-track suppression over the Western North Pacific from a cyclone life-cycle perspective. Weath. and. *Climate Dynamics*, *2*(1), 55–69. https://doi.org/10.5194/wcd-2-55-2021

Shaw, T. A., Baldwin, M., Barnes, E. A., Caballero, R., Garfinkel, C. I., Hwang, Y. T., et al. (2016). Storm track processes and the opposing influences of climate change. *Nature Geoscience*, *9*, 656–664. https://doi.org/10.1038/ngeo2783

Simmons, A., Wallace, J., & Branstator, G. (1983). Barotropic wave propagation and instability, and atmospheric teleconnection patterns. *Journal of the Atmospheric Sciences*, *40*(6), 1363–1392. https://doi.org/10.1175/1520-0469(1983)040<1363:bwpaia>2.0.co;2

Simmons, A. J., & Hoskins, B. J. (1978). The life cycles of some nonlinear baroclinic waves. *Journal of the Atmospheric Sciences*, *35*(3), 414–432. https://doi.org/10.1175/1520-0469(1978)035<0414:tlcosn>2.0.co;2

Tamarin, T., Heifetz, E., Umurhan, O. M., & Yellin, R. (2015). On the nonnormal–nonlinear interaction mechanism between counter-propagating Rossby waves. *Theoretical and Computational Fluid Dynamics*, *29*(3), 205–224. https://doi.org/10.1007/s00162-015-0346-9

Tamarin, T., & Kaspi, Y. (2016). The poleward motion of extratropical cyclones from a potential vorticity tendency analysis. *Journal of the Atmospheric Sciences*, *73*(4), 1687–1707. https://doi.org/10.1175/jas-d-15-0168.1

Tamarin, T., & Kaspi, Y. (2017). Mechanisms controlling the downstream poleward deflection of midlatitude storm tracks. *Journal of the Atmospheric Sciences*, *74*(2), 553–572. https://doi.org/10.1175/jas-d-16-0122.1

Tamarin-Brodsky, T., & Hadas, O. (2019). The asymmetry of vertical velocity in current and future climate. *Geophysical Research Letters*, *46*(1), 374–382. https://doi.org/10.1029/2018gl080363

Tamarin-Brodsky, T., & Kaspi, Y. (2017). Enhanced poleward propagation of storms under climate change. *Nature Geoscience*, *10*(12), 908–913. https://doi.org/10.1038/s41561-017-0001-8

Tsopouridis, L., Spensberger, C., & Spengler, T. (2021). Cyclone intensification in the Kuroshio region and its relation to the sea surface temperature front and upper-level forcing. *Quarterly Journal of the Royal Meteorological Society*, *147*(734), 485–500. https://doi.org/10.1002/qj.3929

Vallis, G. K. (2017). *Atmospheric and oceanic fluid dynamics*. Cambridge Univ. Press.

Weijenborg, C., & Spengler, T. (2020). Diabatic heating as a pathway for cyclone clustering encompassing the extreme storm dagmar. *Geophysical Research Letters*, *47*(8), e2019GL085777. https://doi.org/10.1029/2019gl085777

Yau, A. M.-W., & Chang, E. K.-M. (2020). Finding storm track activity metrics that are highly correlated with weather impacts. Part I: Frameworks for evaluation and accumulated track activity. *Journal of Climate*, *33*(23), 10169–10186.